Proceedings 10th NUMGE 2023
10th European Conference on Numerical Methods in Geotechnical Engineering
Zdravkovic L, Kontoe S, Taborda DMG, Tsiampousi A (eds)

https://doi.org/10.53243/NUMGE2023-126

Resonance in offshore wind turbine systems due to seismic loading and extensive soil liquefaction

J.K. Möller[1], S. Kontoe[2], D.M.G. Taborda[1], D.M. Potts[1]

[1]*Department of Civil and Environmental Engineering, Imperial College London, UK*
[2]*Department of Civil Engineering, University of Patras, Greece*

ABSTRACT: Offshore wind turbines in the North Sea are designed to ensure that fundamental frequencies of the turbine-substructure systems lie outside frequency ranges occupied by dynamic wind loads, wave loads and rotor and blade-passing frequencies. For wind farms located in areas of high seismicity, dynamic earthquake loading needs to be further considered to avoid resonance of the wind turbine system. High-intensity seismic ground shaking may lead to liquefaction of sand layers and a reduction in strength and stiffness within the soil. As the stiffness of the ground diminishes, the fundamental period of a deposit may elongate, enabling an amplification of the low-frequency content of an earthquake motion. Through advanced fully-coupled finite element analyses, this study illustrates the example of a 5 MW reference turbine supported by a large diameter monopile founded in a deep soil deposit consisting of stiff marine clay and liquefiable sand. The results show amplification of a strong motion input through a partially liquefied soil deposit within a frequency range near the fixed-based frequency of the turbine tower and illustrate the response of the wind turbine system near resonance.

Keywords: wind turbine foundations; monopile; resonance; liquefaction; period elongation

1 INTRODUCTION

To avoid resonance, wind turbine systems are designed to ensure that the first turbine tower frequencies are not excited by dynamic loads originating from the movement of the rotor (1P), the passing of the blades (3P) and environmental loads. This study considers the example of the representative NREL 5 MW reference turbine by Jonkman et al. (2009), for which the rotor and blade passing frequencies to be avoided lie in the range of $0.15 - 0.22$ Hz (1P) and $0.35 - 0.61$ Hz (3P).

For bottom fixed wind turbines (e.g. monopile foundations), the most common design approach is termed 'soft-stiff'. In this case, the system exhibits a 'stiffer' response with a higher fundamental frequency than the range occupied by the 1P rotor frequencies, while being 'softer' and thus falling below the 3P blade passing frequencies. This design approach further ensures that resonance is not triggered by dynamic wind and wave loads, which are characterised by longer periods. The NREL 5 MW turbine tower frequencies associated with the 1st bending mode in the side-side and in the fore-aft direction are placed near 0.3 Hz.

Earthquake records obtained at rock sites or stiff soil sites typically show dominant frequency contents of horizontal components which lie in a higher range, above 1.0 Hz. Due to their relatively low fundamental frequencies, it is therefore often assumed that wind turbines are not vulnerable to horizontal ground shaking resulting from low intensity earthquakes.

For vibration modes excited by vertical components of earthquake motions, it is already known that this assumption cannot be made (Kaynia, 2018). The focus in this study remains on horizontal vibrations caused by the propagation of shear waves, for which the effects of high-intensity motions and the dynamic response of liquefiable soil deposits are illustrated. Numerical analyses of deep soil deposits are presented which indicate a shift of the frequency content for different input motions. The period elongation observed in the ground response is attributed to a significant reduction in soil stiffness as the ground experiences extensive liquefaction.

2 SOIL PARAMETERS

Two geomaterials are considered in the analyses, the first being Fraser River sand, a well-characterised liquefiable soil. Based on a comprehensive set of monotonic tests available in the literature (e.g. Thomas, 1992) and undrained cyclic simple shear tests (Sivathayalan, 1994), a modified bounding surface plasticity model developed by Tsaparli (2017) was calibrated (Möller, 2022). The focus hereby lies on capturing the cyclic resistance of the sand for a wide range of initial confining pressures to predict the extent of liquefaction in very deep soil deposits. The resulting set of material parameters is presented in Table 1. Additional properties required for the fully-coupled dynamic finite element analyses are the saturated bulk unit weight of the sand,

$\gamma = 19.04\,\mathrm{kN/m^3}$, and the hydraulic conductivities, $\mathrm{k} = 4.433 \times 10^{-4}\,\mathrm{m/s}$ for a relative density $D_\mathrm{r} = 54\,\%$ and $k = 3.647 \times 10^{-4}\mathrm{m/s}$ for $D_\mathrm{r} = 73\,\%$.

Table 1. Fraser River sand material parameters

Model components	Parameters			
Critical state line	p'_{ref}	100.0 kPa	$e_{\mathrm{cs,ref}}$	1.056
	λ	0.04	ξ	0.70
Surfaces	M_c^c	1.38	M_e^c	1.00
	k_c^b	1.60	k_c^d	1.32
	m	0.01	p'_{YS}	1.0 kPa
Flow rule	A_0	1.00	$A_{0,\mathrm{min}}$	0.0
	$p'_{0,\mathrm{A}}$	0.0	b_d	0.0
	d_1	5.0	d_2	0.0
	d_3	0.0	b_{max}	5.0
Nonlinear elasticity	B	422.0	a_1	0.44
	κ	2.0	γ_1	7.95×10^{-4}
	ν	0.2		
Hardening modulus	h_0	0.8	γ	1.0
	μ	-0.40	e_{max}	0.97
	α	1.0	β	0.0
Fabric tensor	H_0	5000.0	ζ	0.0
	H_{max}	5000.0	C_f	200.0

The second material is Cowden till, a stiff marine clay which is simulated using an enhanced modified Cam Clay model with a Hvorslev surface (Tsiampousi et al., 2013) in combination with a nonlinear elastic small strain stiffness model IC.G3S (Taborda and Zdravkovic, 2012), the latter is able to capture the hysteretic response of the soil under cyclic loading. The calibration is described in detail in Zdravkovic et al. (2020) and Burd et al. (2016), with a summary of the resulting material parameters being provided in Table 2. The saturated unit weight is $\gamma = 21.19\,\mathrm{m/s^3}$ and the hydraulic conductivity is $k = 2.0 \times 10^{-10}\,\mathrm{m/s}$.

Table 2. Cowden till material parameters

Model components	Parameters			
Strength	X	0.548	Y	0.698
	Z	0.100		
Nonlinear Hvorslev surface:				
Shape	α	0.25	n	0.40
Plastic potential	β	0.20	m	1.00
Virgin consolidation line:	ν_1	2.20	λ	0.115
Nonlinear elasticity:				
Swelling behaviour	κ	0.021		
Small-strain shear modulus	G_0^*	110.0 MPa	p'_{ref}	100.0 kPa
Shear stiffness degradation	a	9.78×10^{-5}	b	0.987
	$R_{\mathrm{G,min}}$	0.05		
Cyclic loading	$d_{\mathrm{G},1}$	5.78	$d_{\mathrm{G},2}$	5.67×10^{-3}
	$d_{\mathrm{G},3}$	794.01	$d_{\mathrm{G},4}$	0.56

Lastly, a variable hydraulic conductivity formulation by Tsaparli (2017) based on Taborda (2011) was adopted for both sand layers in the pile simulations, with model parameters $r_\mathrm{p}^* = 0.9$, $x_\mathrm{k} = 10$, $n_\mathrm{k} = 10$ and $p'_{0,\mathrm{lim}} = 15\,\mathrm{kPa}$ (Möller, 2022). This feature was introduced to account for an increased hydraulic conductivity in the liquefied soil and to capture co-seismic settlements, which is not further elaborated in this study for the sake of brevity.

3 PERIOD ELONGATION IN DEEP SAND DEPOSITS DUE TO LIQUEFACTION

The simulation of complex soil-structure interaction phenomena of offshore monopile foundations requires the use of advanced three-dimensional analyses. However, such analyses are computationally expensive and therefore not convenient for the investigation of the system response for multiple different earthquake motions. A preliminary study is therefore presented which considers first the free-field response of a deep sand deposit subjected to various seismic base excitations.

3.1 Numerical site response analyses

As displayed in Figure 1, the idealised 100 m deep deposit consists of two layers of Fraser River sand with relative densities of 54 % and 73 %. An earth pressure coefficient at rest of $K_0 = 0.5$ is assumed in the initial state of the analyses.

Presented alongside the stratigraphy are the boundary conditions adopted in the analyses, as well as the discretisation of the finite element model. The mesh consists of eight-noded quadrilateral isoparametric elements with pore pressure degrees of freedom assigned at the corner nodes and displacement degrees of freedom at all corner and mid-side nodes. For further details on the finite element software ICFEP, the reader may refer to Potts and Zdravković (1999), explanations of dynamic time integration schemes can be found in Kontoe (2006). In the following analyses, the generalised α-scheme by Chung and Hulbert (1993) is adopted with numerical parameters $\beta_{\mathrm{dyn}} = 0.3025$, $\gamma_{\mathrm{dyn}} = 0.506$, $a_\mathrm{m} = 0.35$, $a_\mathrm{f} = 0.35$.

Each motion is imposed at the base through incremental displacement-controlled boundary conditions in the horizontal direction, while any movement in the vertical direction is fixed. Along the height of the soil column, horizontal and vertical displacements are tied at nodes of the same elevation. Pore pressure degrees of freedom are similarly tied between the vertical mesh boundaries to ensure that the simulated response is representative of free-field conditions. The base and lateral boundaries are modelled as impermeable, while a zero-change in pore pressure condition at the surface allows water to be discharged.

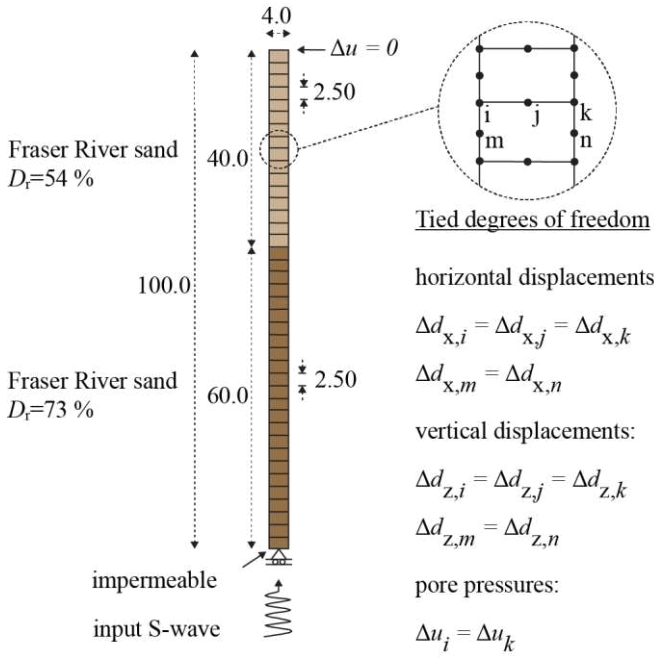

Figure 1. Stratigraphy, finite element mesh and boundary conditions (all dimensions in [m])

Six earthquake motions were selected and, where necessary, scaled in order to match or exceed the four design spectra included in Figure 2 over a significant period range. The latter were generated for sites in West Taiwan (Chai and Teng, 2012), Los Angeles (ASCE, 2013), Japan (Kuramoto, 2006) and West Canada (ISO, 2017), aiming to represent various seismic areas where wind farm developments may potentially be located.

All motion records are listed in Table 3 alongside information on the component used, applied scaling factors, peak ground acceleration (PGA) of the scaled motion and the duration of each event.

Table 3. Strong motion records used as dynamic base excitations

Motion (component)	RSN PEER	Scaling	PGA [g]	Duration [s]
Tabas 1978 (EW)	143	0.4	0.37	33.0
Chamoli 1999 (EW)	-	1.0	0.37	24.3
Kobe 1995 (EW)	1111	1.0	0.49	40.9
Kocaeli 1999 (EW)	1165	1.5	0.33	30.0
Manjil 1990 (EW)	1633	1.0	0.49	46.0
Parkfield 2004 (NS)	4097	1.0	0.37	21.2

Five of the original records were obtained from the strong motion database PEER (2014), where they are uniquely identifiable by their record sequence number (RSN). The Chamoli earthquake can be found in the COSMOS (2005) database, recorded on the 28th of March 1999 at 19:05:11 UTC at the IITR station in Gopeshwar. All motions were quadratically baseline corrected and subjected to a 4th Butterworth filter passing frequencies between 0.1 and 25.0 Hz using the software SeismoSignal. A timestep of 0.02 s was selected for each of the six records to ensure sufficient accuracy.

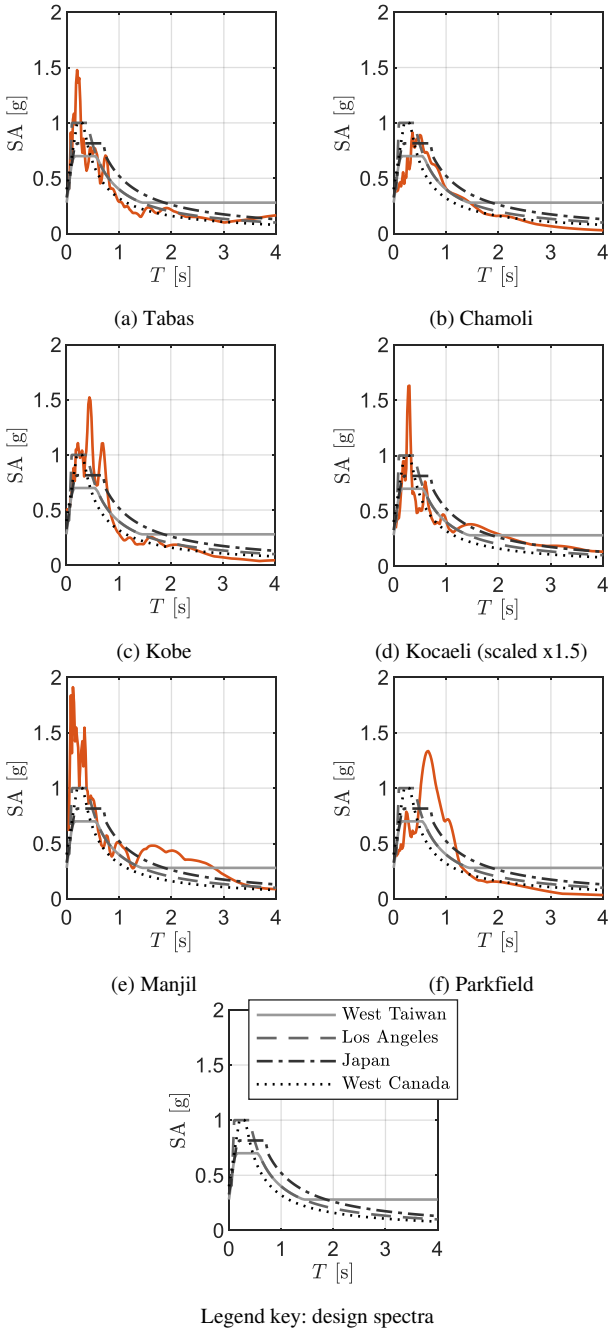

Figure 2. Spectral acceleration of various strong motions for 5 % damping (orange) against design spectra from highly seismic areas

3.2 *Dynamic response of a liquefiable deep sand deposit*

All shaking events lead to substantial liquefied zones, which extend from the ground surface to various depths. Inside these zones, a state of near-zero mean effective stress is reached. The maximum depths of liquefaction are illustrated in Figure 3, which are obtained from time histories of mean effective stress at different depths by plotting the minimum values p'_{min} at each location. The maximum extent of liquefaction induced by each input motion is: (a) 30.0 m, (b) 20.0 m, (c) 12.5 m, (d) 37.5 m, (e) 30.0 m, (f) 15.0.

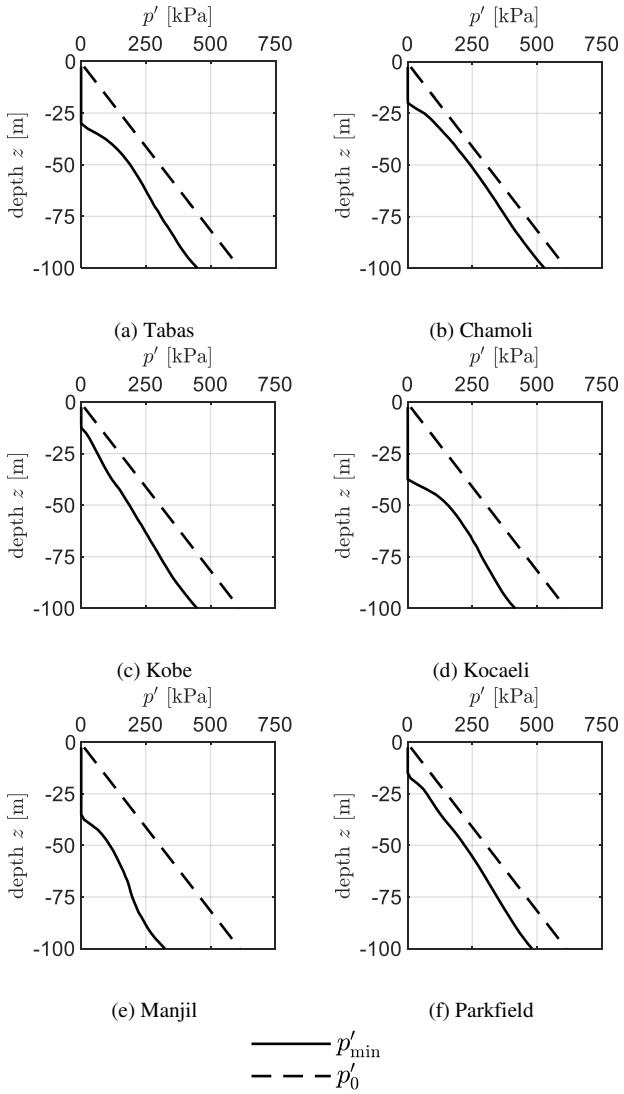

Figure 3. Mean effective stress profiles: initial (p'_0) and minimum (p'_{min})

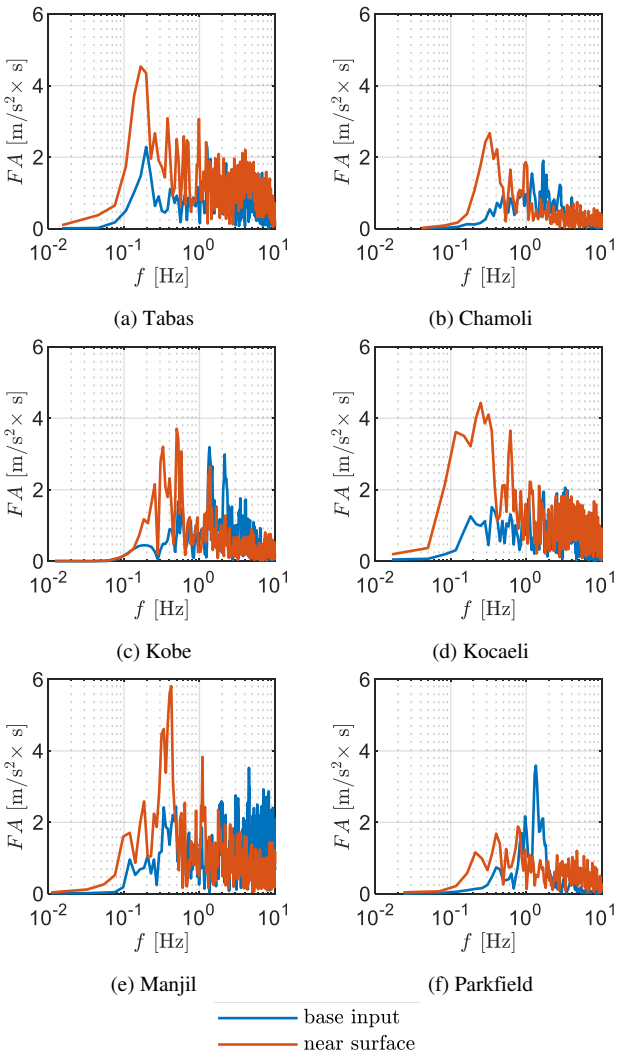

Figure 4. Fourier amplitude spectra of near-surface accelerations ($z = -2.5\ m$) and base excitations ($z = -100.0\ m$)

Within these areas of widespread liquefaction, the shear stiffness of the sand diminishes. This nonlinearity leads to a softer response under dynamic excitation than a stiff, non-liquefiable soil, as will be further illustrated in Section 4.

The comparison of Fourier amplitude spectra of near-surface accelerations with input motions at bedrock level indicates a similar trend for all six events, as shown in Figure 4. Frequency components higher than 1 Hz are not significantly amplified in all cases. On the contrary, during the Chamoli, Kobe, Manjil and Parkfield earthquake, the higher frequency content is notably de-amplified.

However, significant peaks in the near surface response are visible in the range between $0.2 - 0.5$ Hz. A strong response in the lower frequency range can be expected as a result of period elongation due to liquefaction. This can further pose a threat of exciting fundamental modes of vibration for long and slender superstructures, such as wind turbines installed in liquefiable ground.

4 RESONANCE OF A WIND TURBINE

The impact of low frequency amplification in liquefiable deposits is illustrated for the 5 MW reference turbine (Jonkman et al., 2009), which is supported by a transition piece and monopile foundation. The geometry of the turbine and transition piece is simplified and a constant diameter equal to that of the monopile is modelled over the entire height of the system. The wall thicknesses (t) and densities (ρ) of each component are adjusted accordingly to ensure the same distribution of mass and flexural rigidity as the reference turbine. Furthermore, the ground stratigraphy detailed in Figure 5 includes a bottom layer of Cowden till. This helps to illustrate the modification of the motion's frequency content as shear waves propagate through soft liquefied sand as well as a stiff clay layer.

4.1 Material properties (structural parts)

Shell elements are used to model the turbine tower ('T'), transition piece ('TP'), monopile ('P') and the connection between the latter two ('CON'). All structural parts

are indicated alongside the system dimensions in Figure 5. The corrected densities ρ and wall thicknesses t for each part are: $\rho_P = 7.85$, $\rho_{CON} = 10.54$, $\rho_{TP} = 10.29$ in [g/cm^3] and $t_P = 91.35$, $t_{CON} = 119.8$, $t_{TP} = 55.52$ in [mm]. The properties along the turbine tower are scaled and linearly interpolated between the 'top' and 'base' to account for its tapered shape: $\rho_{T,top} = 40.24$, $\rho_{T,base} = 17.63$ in [g/cm^3] and $t_{T,top} = 2.550$, $t_{T,base} = 11.664$ in [mm]. Young's modulus ($E = 210$ GPa) and Poisson's ratio ($\nu = 0.3$) are identical for all steel parts. Zero-thickness interface elements characterised by a friction angle $\phi' = 32°$, *c*ohesion $c' = 0$ kPa and elastic stiffness properties $K_N = K_S = 1.0 \times 10^5$ kN/m^3 in normal and transverse direction are employed to simulate the slip between the pile wall and the adjacent soil. The rotor nacelle assembly (RNA) is represented by a lumped mass of 350 tons centred at hub level at the turbine tower top.

4.2 *Numerical 3D analyses for a simplified wind turbine-monopile system*

Due to symmetry, it is possible to model only half of the problem, as shown in Figure 5, and thus significantly reduce the computational cost of the analysis. All boundary conditions applied at the base of the mesh, across the soil surface, at the back- and at the two vertical side boundaries are analogous to the free-field boundary conditions previously described for the one-dimensional site response analyses. At the plane of symmetry, i.e. the front boundary, movement in y-direction is restricted. Along the vertical edges of the half-tubular turbine tower and sub-structure, rotational fixities around the x- and z-axis are applied to ensure that the shell elements remain perpendicular to the plane of symmetry.

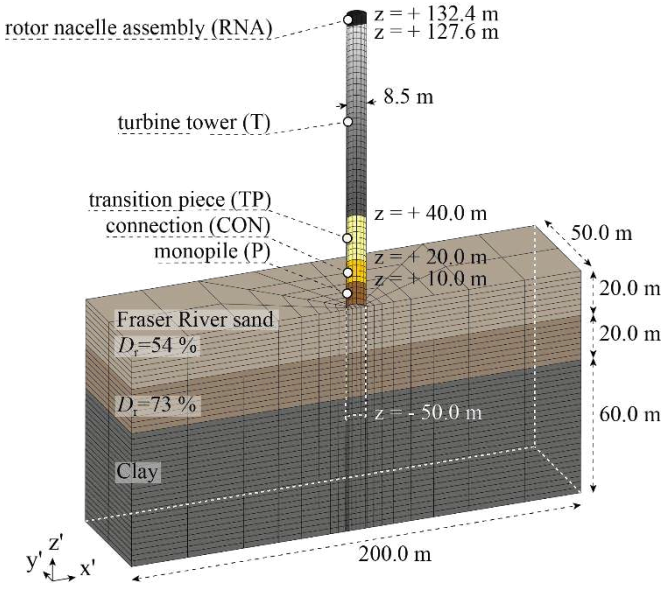

Figure 5. Simplified turbine substructure system: geometry, ground stratigraphy and finite element mesh

The east-west component of the 1995 Kobe earthquake (Table 3) is applied as a base input excitation in x-direction. A dissipative version of the Newmark (1959) algorithm is adopted for the dynamic time integration scheme, with parameters $\beta_{dyn} = 0.3025$ and $\gamma_{dyn} = 0.6$. K_0- and OCR-profiles used to initialise the analyses are displayed in Figure 6.

4.3 *Dynamic response of the far-field ground deposit and the turbine at hub level*

A snapshot of the computed minimum mean effective stress profile at time $t = 21$ s is presented alongside the initial stress profile in Figure 6(c), corresponding to the maximum extent of liquefaction. At this instant, the entirety of the sand layers comprising the top 40 m of the deposit is fully liquefied.

Figure 7 displays the Fourier amplitude spectra for free-field accelerations at various depths: near the ground surface (−2.5 m), between the three soil layers (−20.0 m and −40.0 m) and at the base (−100.0 m).

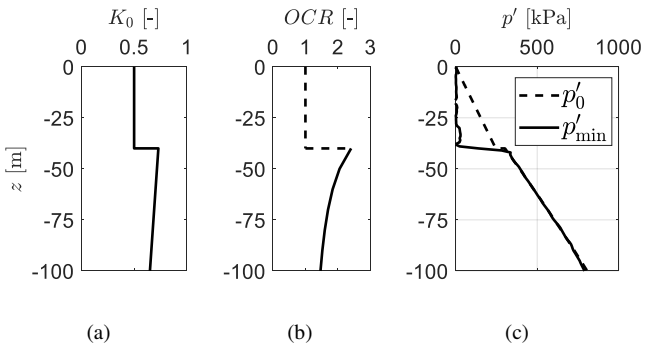

Figure 6. (a) Initial K_0-profile, (b) OCR-profile used in enhanced MCC model, (c) effective stress profile at the initial state and at $t = 21$ s along left-hand side mesh boundary

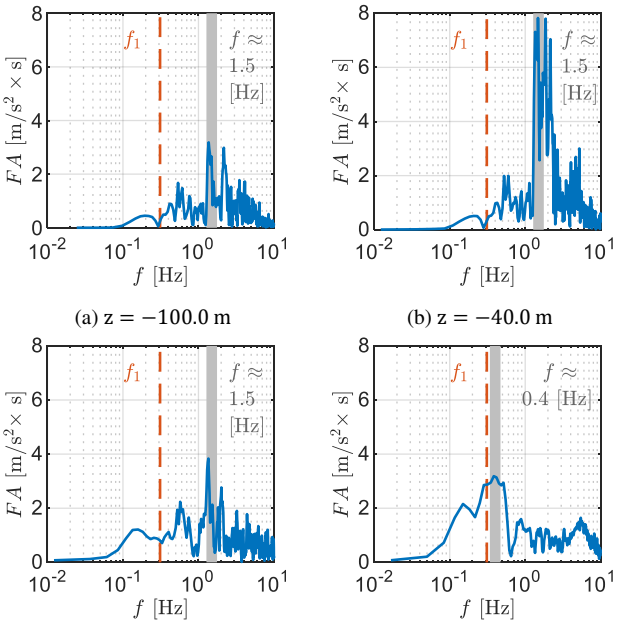

Figure 7. Fourier amplitude spectra at various depths across the soil profile against the 1st turbine tower frequency

The free-field accelerations are obtained from the left-hand side mesh boundary and their predominant frequencies are indicated in grey in Figure 7. From the base excitation shown in Figure 7(a) to the top of the stiff clay strata at $z = -40.0$ m (Figure 7(b)), the motion is strongly amplified near the peak input frequency of 1.5 Hz. Further up into the liquefied sand layers, a gradual shift to lower frequencies can be observed in the ground response. Most notably near the soil surface at $z = -2.5$ m, the motion is dominated by frequency components near 0.4 Hz. Included for comparison is the first fixed-base turbine tower frequency f_1 of the side-side vibration mode, which lies in close proximity to this peak at 0.31 Hz (Jonkman et al., 2009).

The acceleration of the RNA mass at the top of the wind turbine tower is presented in time- and frequency domains in Figure 8. Compared to the fixed-base turbine tower frequencies of the 1st and 2nd modes of vibration after Jonkman et al. (2009), an elongation of periods is expected due to the compliance of the soil-foundation system. The results not only show an excitation of the second vibration mode, but also a strong response near the first resonance frequency of the turbine tower.

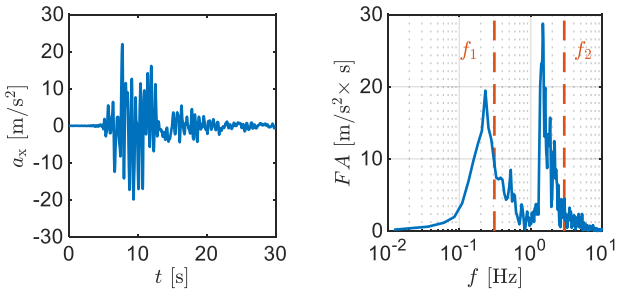

Figure 8. Turbine tower top response: (a) time history and (b) Fourier amplitude spectra against first ($f_1 = 0.31$ Hz) and second ($f_2 = 2.94$ Hz) fixed-based tower frequencies of the reference turbine

5 CONCLUSIONS

This study highlights how low frequency components of seismic shear waves propagating through deep deposits can be amplified due to extensive soil liquefaction. The resonant frequency of wind turbine towers, which are generally assumed not be vulnerable to low intensity earthquakes, may therefore be excited during strong motion events that induce significant nonlinearity in the soil surrounding monopile foundations.

6 REFERENCES

ASCE 2013. Minimum Design Loads for Buildings and Other Structures (ASCE 7-10), 7-10.

Burd, H., Houlsby, G., Martin, C., McAdam, R., Beuckelaers, W., Zdravkovic, L., Taborda, D., Potts, D., Jardine, R., Gavin, K., Igoe, D. 2016. PISA Project - Damping Project Report (No. 2485126A).

Chai, J.-F., Teng, T.-J. 2012. Seismic Design Force for Buildings in Taiwan. *15 World Conference on Earthquake Engineering, Lisbon*.

Chung, J., Hulbert, G.M. 1993. A Time Integration Algorithm for Structural Dynamics With Improved Numerical Dissipation: The Generalized-α Method. *Journal of Applied Mechanics* **60**, 371–375.

COSMOS 2005. The COSMOS Virtual Data Center. Consortium of Organizations for Strong-Motion Observation Systems (COSMOS).

ISO 2017. Petroleum and natural gas industries - Specific requirements for offshore structures - Part 2: Seismic design procedures and criteria (ISO 19901-2:2017), 2nd ed.

Jonkman, J., Butterfield, S., Musial, W., Scott, G. 2009. Definition of a 5-MW Reference Wind Turbine for Offshore System Development (No. NREL/TP-500-38060, 947422).

Kaynia, A.M. 2018. Seismic considerations in design of offshore wind turbines. *Soil Dynamics and Earthquake Engineering* **124**, 399–407.

Kontoe, S. 2006. *Development of time integration schemes and advanced boundary conditions for dynamic geotechnical analysis* (PhD thesis). Imperial College London.

Kuramoto, H. 2006. Seismic Design Codes for Buildings in Japan. J. Disaster Res. 1, 341–356.

Möller, J.K. 2022. *Seismic response of monopile foundations for offshore wind turbines in liquefiable deposits* (PhD thesis). Imperial College London.

Newmark, N.M. 1959. A Method of Computation for Structural Dynamics. *J. Engrg. Mech. Div.* **85**, 67–94.

PEER 2014. Pacific Earthquake Engineering Research Center, University of California Berkley.

Potts, D., Zdravković, L. 1999. *Finite element analysis in geotechnical engineering: theory*. Thomas Telford Publishing, London, UK.

Sivathayalan, S. 1994. *Static, Cyclic and Post Liquefaction Simple Shear Response of Sands* (MSc thesis). University of British Columbia.

Taborda, D.M.G. 2011. *Development of Constitutive Models for Application in Soil Dynamics* (PhD thesis). Imperial College London, London.

Taborda, D.M.G., Zdravkovic, L. 2012. Application of a Hill-Climbing technique to the formulation of a new cyclic nonlinear elastic constitutive model. *Computers and Geotechnics* **43**, 80–91.

Thomas, J. 1992. *Static, cyclic and post liquefaction undrained behaviour of Fraser River sand* (MSc thesis). University of British Columbia.

Tsaparli, V. 2017. *Numerical modelling of earthquake-induced liquefaction under irregular and multi-directional loading* (PhD thesis). Imperial College London.

Tsiampousi, A., Zdravković, L., Potts, D.M. 2013. A new Hvorslev surface for critical state type unsaturated and saturated constitutive models. *Computers and Geotechnics* **48**, 156–166.

Zdravković, L., Taborda, D.M.G., Potts, D.M., Abadias, D., Burd, H.J., Byrne, B.W., Gavin, K.G., Houlsby, G.T., Jardine, R.J., Martin, C.M., McAdam, R.A., Ushev, E. 2020. Finite-element modelling of laterally loaded piles in a stiff glacial clay till at Cowden. *Géotechnique* **70**, No. 11, 999-1013.